AGU PUBLICATIONS

JGR

Journal of Geophysical Research: Solid Earth

RESEARCH ARTICLE
10.1002/2014JB011391

Key Point:
- First 3-D velocity field inversion of InSAR and GPS of the entire Afar depression shows that plate spreading in Afar is currently achieved in contrasting modes, coexistence of transient postdiking processes, but also distributed spreading

Supporting Information:
- Readme
- Figures S1–S18

Correspondence to:
C. Pagli,
carolina.pagli@unipi.it

Citation:
Pagli, C., H. Wang, T. J. Wright, E. Calais, and E. Lewi (2014), Current plate boundary deformation of the Afar rift from a 3-D velocity field inversion of InSAR and GPS, *J. Geophys. Res. Solid Earth*, *119*, 8562–8575, doi:10.1002/2014JB011391.

Received 16 JUN 2014
Accepted 28 OCT 2014
Accepted article online 30 OCT 2014
Published online 28 NOV 2014

This is an open access article under the terms of the Creative Commons Attribution License, which permits use, distribution and reproduction in any medium, provided the original work is properly cited.

Current plate boundary deformation of the Afar rift from a 3-D velocity field inversion of InSAR and GPS

Carolina Pagli[1,2], Hua Wang[3], Tim J. Wright[4], Eric Calais[5], and Elias Lewi[6]

[1]School of Earth and Environment, University of Leeds, Leeds, UK, [2]Dipartimento di Scienze della Terra, Università di Pisa, Pisa, Italy, [3]Department of Surveying Engineering, Guangdong University of Technology, Guangzhou, China, [4]COMET, School of Earth and Environment, University of Leeds, Leeds, UK, [5]Ecole Normale Supérieure, PSL Research University, Paris, France, [6]IGSSA, Addis Ababa University, Addis Ababa, Ethiopia

Abstract Extension, faulting, and magmatism are the main controls on the magnitude and localization of strain at mid-ocean ridges. However, the temporal and spatial patterns of such processes are not clear since the strain distribution has not been resolved in the past at sufficient spatial resolution and over extended areas. Interferometric synthetic aperture radar (InSAR) and GPS data with unprecedented resolution are now available to us from the Afar rift of Ethiopia. Here we use a velocity field method to combine InSAR and GPS to form the first high-resolution continuous three-dimensional velocity field of Afar. We study an area that is 500 km wide and 700 km long, covering three branches of the Afar continental rift and their triple junctions. Our velocity field shows that plate spreading is currently achieved in Afar in contrasting modes. A transient postdiking deformation is focused at the Dabbahu rift segment, while in central Afar, spreading is distributed over several overlapping segments and southern Afar exhibits an interdiking deformation pattern focused at the Asal–Ghoubbet segment. We find that current spreading rates at Dabbahu, following the 2005–2010 intrusions, are up to 110 mm/yr, 6 times larger than the long-term plate divergence. A segment-centered uplift of up to 80 mm/yr also occurs, indicating that magma flow is still a primary mechanism of deformation during postdiking. On the other hand, no vertical displacements are currently observed in central and southern Afar, suggesting lack of significant magmatic activity at shallow levels.

1. Introduction

Established plate spreading is cyclical; the rates and spatial distribution of strain vary greatly during each phase of the cycle, as different tectonic and magmatic mechanisms control the deformation [*Sigmundsson*, 2006; *Wright et al.*, 2012]. The cyclicity of plate spreading has been appreciated following diking events at a few places: in Krafla (Iceland, 1975–1984), in Asal–Ghoubbet (Djibouti, 1978), and Dabbahu (Afar, 2005–2010) [*Sigmundsson*, 2006; *Vigny et al.*, 2007; *Wright et al.*, 2012]. Three phases have been identified during a full plate spreading cycle: interdiking, codiking, and postdiking. During the interdiking phase, extension across the plate margin is steady, gradually building up tensile stresses in the elastic layer. These stresses are then released through repeated dike injections and eruptions (codiking phase) [e.g., *Wright et al.*, 2006]. A transient postdiking period follows, with extension across the plate margin occurring at a rate several times higher than the long-term spreading rate [e.g., *Foulger et al.*, 1992].

The transient postdiking deformation has been explained assuming two different mechanisms. In Iceland, it has been largely explained by the slow relaxation of stresses induced in the ductile part of the crust and mantle by earlier dike intrusions in the elastic layer [*Foulger et al.*, 1992; *Heki et al.*, 1993; *Hofton and Foulger*, 1996]. Conversely, both viscoelastic stress relaxation [*Vigny et al.*, 2007] and magma flow into the deep crust [*Cattin et al.*, 2005] have been invoked as the cause of the accelerated deformation following the 1978 Asal–Ghoubbet episode. In Afar, the onset of the rifting episode in 2005 was marked by a large magma intrusion (2–2.5 km^3) such that has caused the initiation of a postdiking phase. At the same time, repeated intrusions have also continued occurring during the 2005–2010 time period, further contributing to the postdiking deformation. The postdiking deformation has been modeled assuming either viscoelastic stress relaxation or continued dike injection at depth [*Grandin et al.*, 2010; *Nooner et al.*, 2009] as well as a combination of stress relaxation and inflation/deflation of magma chambers [*Hamling et al.*, 2014].

Afar has been created by the separation of the Nubian, Arabian, and Somalian Plates during the past 30 Ma (Figure 1a) [*Barberi and Varet*, 1977; *Courtillot*, 1980; *Ebinger et al.*, 2010]. Extension occurs along three rift

©2014. The Authors.

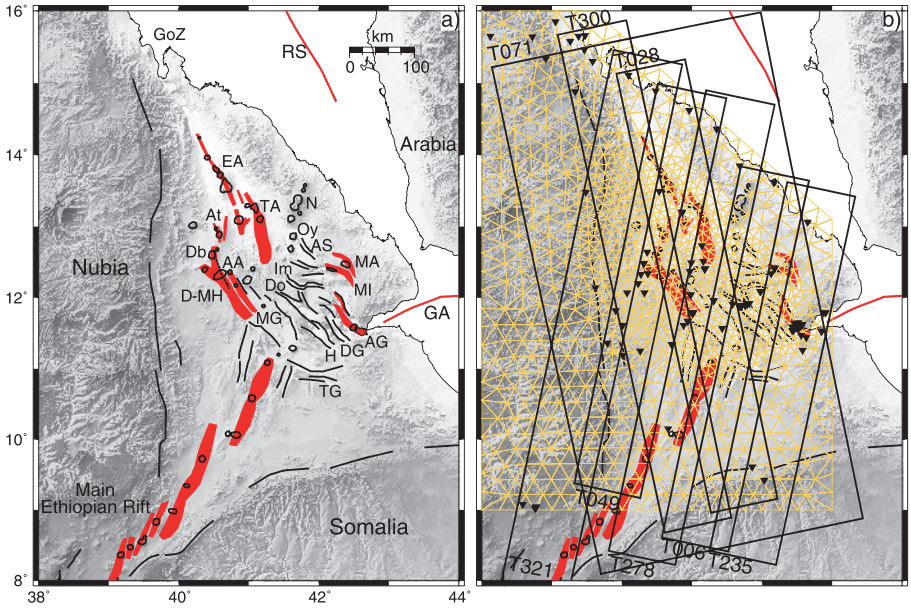

Figure 1. Afar region. (a) The red fillings are the magmatic rift segments: EA (Erta Ale), TA (Tat Ale), At (Alayta), D-MH (Dabbahu–Manda Hararo), AG (Asal–Ghoubbet), MI (Manda-Inakir), and MA (Moussa-Alli). The black lines are amagmatic rift segments: AS (Akulle–Sarodda), Im (Immino), Do (Dobi), MG (Manda Gargori), H (Hanle), and DG (Derela–Gaggade). The black outlines mark the volcanoes: N (Nabro), Db (Dabbahu), AA (Ado Ale), and Oy (Oyma). The dashed line along D-MH marks the area intruded by the 2005–2010 dikes. TG is the Tendaho-Gobha fault, and the Afar region is bounded by border faults (black lines). RS is the Red Sea ridge and GA is the Gulf of Aden ridge. GoZ indicates the gulf of Zula. (b) Data set and mesh used in the 3-D velocity field inversion. The black rectangles mark the InSAR tracks; the black triangles are the GPS sites operated by NSF and the Afar Rift Consortium [*McClusky et al.*, 2010; *Kogan et al.*, 2012; *Vigny et al.*, 2006, 2007; *Saria et al.*, 2013].

branches, the Red Sea, the Gulf of Aden, and the Main Ethiopian Rift. Current full spreading velocities are 18 mm/yr between Nubia and Arabia, 16 mm/yr for the Somalian–Arabian Plates, and 6 mm/yr for Nubia–Somalia [*McClusky et al.*, 2010; *Saria et al.*, 2014; *Vigny et al.*, 2006]. Since ~3 Ma, the central axis of the plate boundary in Afar is marked by a series of rift segments, some of which have been volcanically active (red outlines in Figure 1a), while others are purely tectonic structures (black lines in Figure 1a). South of 15°N, the onland continuation of the Red Sea Rift in Afar is marked by a lineament of active volcanoes [*Field et al.*, 2012; *Nobile et al.*, 2012; *Pagli et al.*, 2012; *Wright et al.*, 2012] that can be traced to ~12°N. However, the mode by which a connection between the Red Sea and the Gulf of Aden rifts is realized in southern Afar remains unclear. A possible model is one of rift propagation together with block rotations [*Kidane et al.*, 2003; *Manighetti et al.*, 1998; *Tapponnier et al.*, 1990].

Interferometric synthetic aperture radar (InSAR) has the ability to measure displacements at high accuracy (subcentimeter) and over large areas (~100 km), but measurements are one-dimensional, and extracting the three-dimensional displacement field remains challenging. Previous attempts to obtain the across-rift horizontal and the vertical components in Dabbahu have involved combining InSAR images from different orbits [*Hamling et al.*, 2014]. The limitations of this method are that two components of the displacement field can be separated only in the overlapping area of the two sets of images, losing the InSAR spatial coverage, and that assumptions have to be made about the orientation of deformation, for example that there is no north-south (or rift parallel) motion [*Wright et al.*, 2004]. This assumption is not ideal for concentric deformation at volcanoes where the north-south component of the displacement will be mapped in apparent vertical motion.

In this paper we combine all available GPS data with InSAR from eight tracks in a common reference frame, using the method of *Wang and Wright* [2012] to derive the first high-resolution continuous 3-D velocity field of the Afar rift (Ethiopia). We are able to capture the kinematic complexity of the plate boundary deformation as well as resolve the current strain distribution at regional scale. In particular, we can capture the full spatial extent of the transient postdiking deformation that follows the onset of the Afar diking event in 2005 in Dabbahu. Furthermore, we identify broad deformations in the rift segments of central Afar and a focused extension in southern Afar, at Asal–Ghoubbet, where the segment is experiencing an interdiking phase.

©2014. The Authors.

2. InSAR and GPS Data Analysis

We analyzed GPS and InSAR data from 2005 to 2010 to reconstruct the plate boundary kinematics of Afar (Figure 1b). Following a two-step approach, we combined InSAR data from multiple tracks together with all available GPS measurements to obtain the three-dimensional velocity field for Afar. First, we obtain the line of sight (LOS) surface velocities for each InSAR track using a multi-interferogram method, π-rate software [*Wang et al.*, 2012]. Second, we combine these with the GPS observations, using the velocity-field method developed by *Wang and Wright* [2012].

2.1. Data

We created about 350 interferograms using images from eight Envisat tracks (006, 028, 049, 071, 235, 278, 300, and 321) in both descending and ascending orbits, in image and wide-swath modes, spanning the period between 2005 and 2010 and covering the whole Afar region (Figure 1b and Figure S1 in the supporting information). The data cover ~350,000 km^2, which is the largest area ever imaged continuously with InSAR.

We used the Jet Propulsion Laboratory (JPL)/California Institute of Technology ROI_PAC software [*Rosen et al.*, 2004] and a 3 arc sec Shuttle Radar Topography Mission digital elevation model (SRTM DEM) to create all the interferograms. We used a standard 20 azimuth and 4 range looks and filtered interferograms using a power spectrum filter before phase unwrapping with the branch-cut method. Phase unwrapping errors were initially identified in each interferogram using the phase closure technique on minimum spanning trees [*Kruskal*, 1956]. They were then manually corrected when the absolute sum of the closure was equal to or larger than 2π. The data were geocoded to the 3 arc sec SRTM DEM (~90 m resolution).

The GPS data set analyzed here includes a total of 112 sites. The GPS sites near Dabbahu–Manda Hararo and in central Afar were measured between 2007 and 2010 as a part of the Afar Rift Consortium and National Science Foundation (NSF) projects [*Nooner et al.*, 2009], while some GPS velocities from the Red Sea coast, the Gulf of Aden, and the Main Ethiopian Rift are from other sources [*Kogan et al.*, 2012; *McClusky et al.*, 2010; *Saria et al.*, 2013; *Vigny et al.*, 2006, 2007]. We combined all GPS velocities in the common International Terrestrial Reference Frame 2008 and then converted the velocities with respect to Nubia using common sites between the different solutions and the Nubia frame as defined by *Saria et al.* [2013]. Horizontal velocities at sites located on stable Nubia fit a single-plate model with a weighted root-mean-square residual of 0.6 mm/yr. Offset corrections were estimated and subtracted from the GPS time series in order to remove the contributions from dike intrusions at Dabbahu so that GPS velocities in this area are representative of postdiking displacements. The examination of GPS position time series corrected for dike intrusions show that for the time interval considered here, displacements are linear with time and can be described by a constant velocity at each site.

2.2. InSAR Time Series Analysis

We obtained time series of cumulative displacements, average velocities, and their associated uncertainties for each InSAR track using the π-rate software. The π-rate software uses a network-based approach on the geocoded interferograms to mitigate common sources of errors in the interferograms, such as orbital and atmospheric delay errors [*Biggs et al.*, 2007; *Elliott et al.*, 2008]. In all our time series analyses, we removed contributions from sudden events (see description in the following) such as those caused by dike intrusions and eruptions.

In this study, the focus is on the regional-scale deformation pattern in Afar. Therefore, we averaged 10 geocoded neighboring pixels to ~900 m resolution in all interferograms, which reduced both the noise and the number of data points. Any unwrapping errors that may have not been manually corrected, as described in section 3.1, were again identified, using the phase closure technique on minimum spanning trees, as implemented in the π-rate software [*Wang et al.*, 2012], and these pixels were automatically excluded from the analysis. Quadratic orbital corrections were applied to all the InSAR tracks, as these have lengths of several hundred kilometers. Linear functions were also tested but provided a worse fit to the data, as have been found elsewhere in large regions [*Wang and Wright*, 2012]. Topographically correlated atmospheric delay errors were estimated and removed using a linear function to the height [*Elliott et al.*, 2008; *Wang et al.*, 2012].

©2014. The Authors.

We removed sudden displacement steps in the time series using a novel cross-correlation method in the time series analysis that we developed for this study. The method has three steps. (i) We invert the interferograms for the raw time series, without smoothing, and then form at least two independent interferograms spanning a given sudden event. (ii) In order to identify the area of the interferogram affected by a sudden deformation, we calculate the cross correlation between the independent interferograms. Areas affected by a sudden deformation are highly correlated, while other areas have low correlation. (iii) For the final step, our aim is to subtract from those interferograms spanning the time of a sudden event, the deformation corresponding to the highly correlated areas but leaving all other areas unchanged (the correlation ranges from 0 to 1 for poorly to highly correlated areas). For this purpose, we used an arctangent function,

$$f = 0.5 + \frac{1}{\pi} \cdot \tan^{-1}[D \cdot (C - C_T)]$$

where C is the correlation value as calculated in step (ii), C_T is a correlation threshold, and D is the slope of the function. We then obtained a residual interferogram (without sudden deformation) according to $\Delta_\varphi = \varphi - f \cdot \varphi$, where φ is the incremental shortest-interval interferogram spanning the event. For values of correlation greater than the threshold, f will approach 1 (for high values of D). Conversely, for low values of correlation, f will be close to 0. Therefore, in the residual interferogram, Δ_φ, most of the correlated deformation will be subtracted, while poorly correlated area will be practically unchanged. Unlike a step, an arctangent function can avoid unrealistic sharp boundaries in the residual interferogram, where C is close to C_T. We found that a C_T between 0.6 and 0.7 was able to reliably identify the areas of coherent sudden deformation present in all interferograms spanning the event. The sharpness of the boundary is controlled by the slope D, with high values removing the correlated signal more strongly than lower values. Different values of correlation coefficient threshold and slope were tested, and the residual interferograms were inspected to ensure that sudden displacements had been removed; we found that D in the range of 20 to 25 gave good results. Moreover, the value of f will be somewhat smaller than 1 even for the strongest correlated signal, as we avoid using too large values of D, which would leave sharp boundaries where C is close to C_T. This implies that after the correction, some sudden deformation is left in the residual interferogram. Therefore, the correlation procedure is applied twice in order to fully remove sudden deformations.

We show in Figure 2 a detailed example of the cross-correlation method, including the individual steps that lead to the removal of the sudden deformation caused by the November 2007 dike intrusion in Dabbahu, using two independent interferograms (Figures 2a and 2b). In Figures 2c and 2d, we show the correlation, C, and the arctangent function, f, respectively, and in Figures 2e and 2f, the result estimated sudden deformation and residual. Since the correlation is applied twice, in Figures 2g–2i, we also show the parameters of the second correlation procedure. Finally, in Figures 2j–2l, we show the final estimated sudden deformation and the residuals for the two independent interferograms. Furthermore, in Figure S2 in the supporting information, we show the results of the cross-correlation method using three independent interferograms covering the March 2008 Dabbahu intrusion. These examples demonstrate the efficiency of the cross-correlation method in removing sudden dike deformations while leaving other signals, such as time-progressive deformations near Hararo, unchanged. In both examples, most of the deformation caused by the intrusions is removed, and we observe no significant improvement in the sudden deformation removal when correlating three rather than two independent interferograms. Although, correlating an increasingly large number of independent interferograms should provide a better identification of the sudden deformation, it might be that the difference between correlating two or three independent interferograms is not significant. Dike intrusions in Dabbahu have occurred at closely spaced time interval such that only in a few cases, it is possible to correlate up to three independent interferograms. More dense satellite acquisitions and creation of larger number of independent interferograms will be possible in the future to further test the selection and number of independent interferograms to be used in the correlation.

A set of observed model and residual interferograms spanning the times of all dike intrusions in Dabbhau is shown in Figure S3 in the supporting information. It must be noticed that this method will remove only episodic displacements when at least one short time spanning interferogram across a given episode is available. If only long-interval interferograms are used, then both sudden displacements and any other signal exceeding the noise level are likely to correlate and hence be removed. Our time series include interferograms spanning the shortest time period, in most cases about a month, across an episodic event. Furthermore, atmospheric noise can be significant in Afar, but the cross-correlation correction is applied before any atmospheric cleaning

©2014. The Authors.

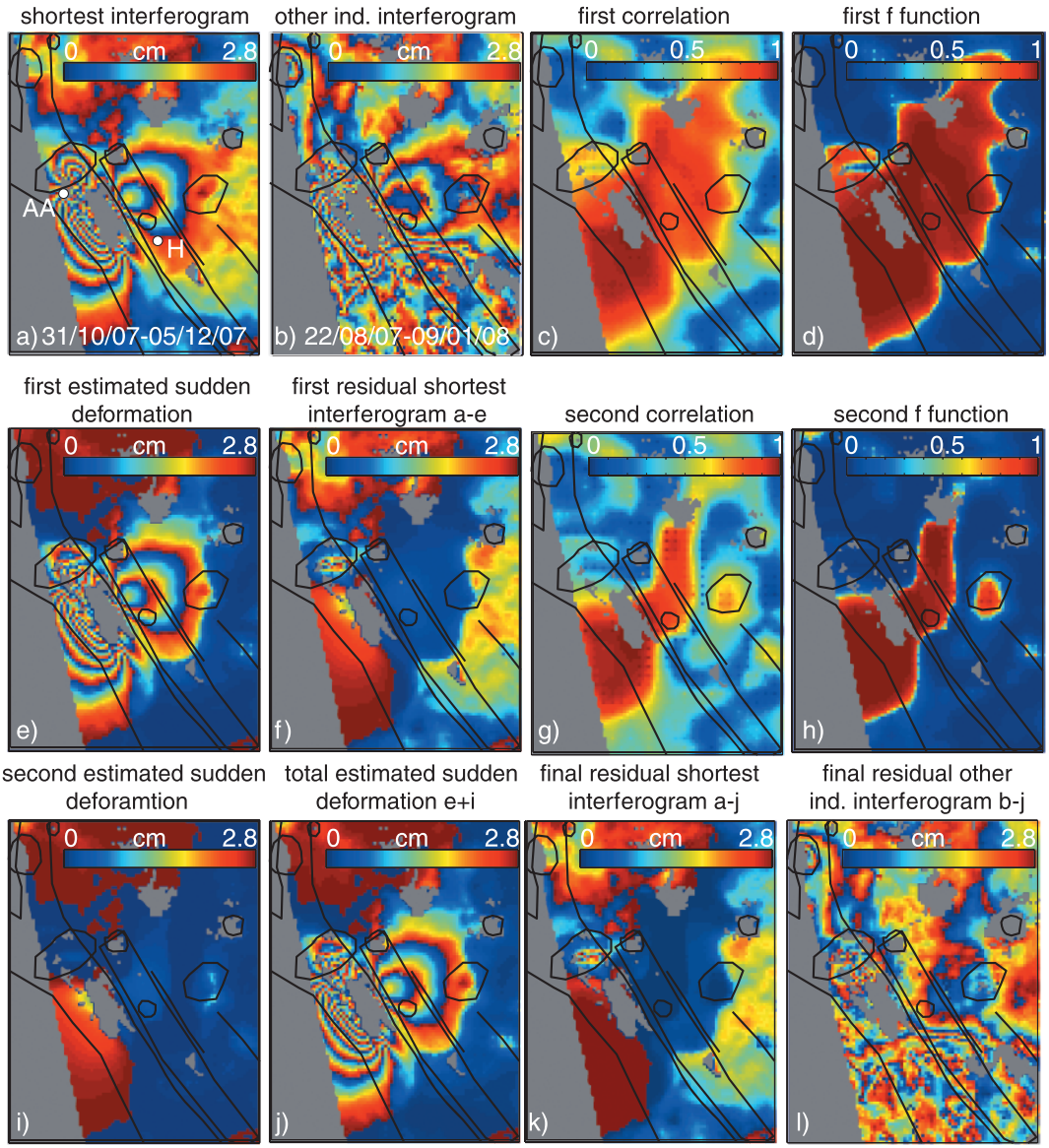

Figure 2. Removal of the displacement caused by the November 2007 intrusion in Dabbahu using the cross-correlation method and two independent interferograms of track 028. (a and b) The two shortest independent interferograms. (c) The correlation, (d) the *f* function, (e) the estimated sudden deformation, and (f) the residual, respectively, after the first correlation are shown. (g–i) The parameters of the second correlation and (j) the total estimated sudden deformation. (k–l) The final residuals for the two shortest independent interferograms. Acquisition dates of the interferograms are marked in Figures 2a and 2b. The letters AA and H mark the positions of Ado Ale and Hararo.

such that only strong deformation signals that exceed the noise level will give a high correlation and be subtracted. Therefore, our average velocity maps can preserve the stable deformation rates, while deformations due to dike intrusions and eruptions are removed. The main advantages of separating steady and sudden deformations with the cross-correlation method are that a priori models of such deformations are not needed nor assumptions about the trend of the steady deformation. Future SAR missions will provide scientists with dense satellite acquisitions making cross-correlation method a potentially efficient way to separate steady and sudden deformation.

Furthermore, we applied atmospheric phase screen (APS) filtering to mitigate atmospheric disturbances. The APS consists of two steps: a temporal high-pass filter followed by a spatial low-pass filter similar to *Ferretti et al.* [2001]. Here we used a Gaussian temporal filter with 1σ of 0.5 years to minimize temporal variations

©2014. The Authors.

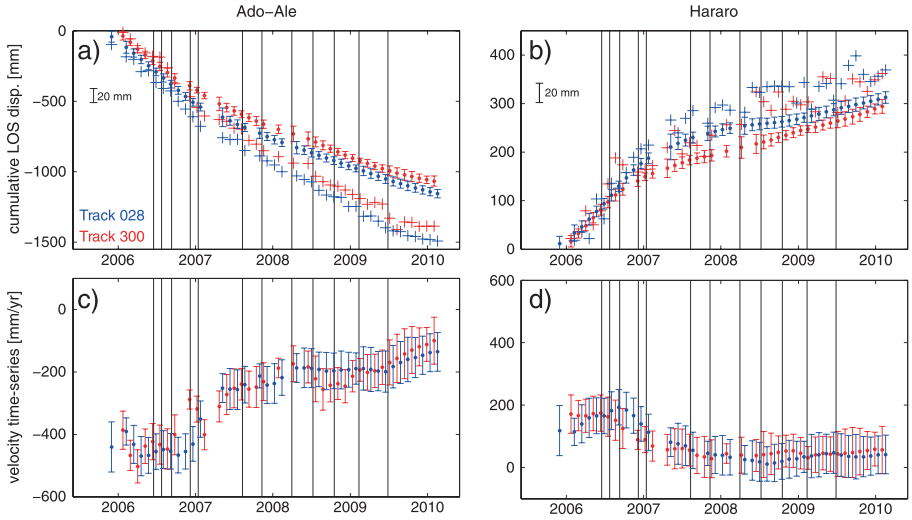

Figure 3. Time series of (a and b) cumulative displacements and (c and d) incremental velocities in the satellite line of sight (LOS) at Ado Ale and Hararo from tracks 028 (blue) and 300 (red). The plus signs show the raw time series (including sudden deformations), and the dots with 2 sigma error bars are the final smoothed time series after the removal of offsets and APS. In Figures 3a and 3b, the error bars are scaled, and the scale is given. The black vertical lines give the time of dike intrusions and eruptions. The positive values indicate the range increase.

shorter than a year as we focus on long-term, steady velocities. We used a Butterworth spatial filter and estimate the variance and covariance using a best fit 1-D covariance function [*Hanssen*, 2001].

Finally, we estimated a least square best fit velocity and its RMS misfit to the interferograms on a pixel-by-pixel basis, using a variance-covariance matrix to account for the spatial and temporal correlation between interferograms [*Biggs et al.*, 2007; *Wang et al.*, 2009]. We exclude unreliable pixels from the velocity maps by removing pixels that are not coherent for at least a set number of independent epochs (between 15 and 20). We also removed pixels with RMS misfits larger than an a priori value, here set to 3–4 mm/yr.

3. InSAR Time Series Results

Initially, we obtained time series of incremental displacement together with average LOS velocities and the associated uncertainties for each InSAR track spanning the longest time period possible (Figure S1 in the supporting information). We show the time-evolving cumulative displacements for points close to the Ado Ale volcano and the Hararo subsidence zone for tracks 028 and 300 (Figure 3 and Figure S4 in the supporting information), which offer long and frequent acquisition histories (Figure S1 in the supporting information). The patterns of cumulative displacements in Figures 3a and 3b show that Ado Ale experienced continuous uplift while Hararo subsided. Our time series show a transient deformation with fastest displacement rates (Figures 3c and 3d) both at Ado Ale and Hararo in early 2006, followed by a rapid decay in late 2006 and approximately linear trends in 2007–2010. More importantly, our velocity time series show the first compelling evidence that the velocity changes at Ado Ale and Hararo were coeval, supporting a possible connection between the two magma systems [*Grandin et al.*, 2010]. Higher melt flow from Hararo to Ado Ale in 2006 may have occurred in response to pressure changes caused by the large initial intrusion (2–2.5 km^3) in October 2005. The cumulative volume of the 14 subsequent intrusions (1 km^3) is less than half of the initial dike, requiring less magma flowing into the system in the later part of the diking event. How the connection between Hararo and Ado Ale is accomplished remains unclear. However, the subsidence at Hararo does not appear to be caused by magma moving from the Hararo system to feed the Dabbahu dike intrusions directly, as our time histories indicate that no significant change in subsidence rate occurred during the repeated intrusions (Figure 3b and Figure S4b in the supporting information). The only significant offset displacement is identified at Hararo during the November 2007 intrusion (plus signs in Figure S4b in the supporting information), but this is the signal from the dike opening that intruded in the southern part of the rift, close to Hararo (Figure 2). Likewise, uplift at Ado Ale follows a smooth trend without any fast replenishment following the intrusions (Figure 3a and Figure S4a in the supporting information). We conclude that velocity changes at

©2014. The Authors.

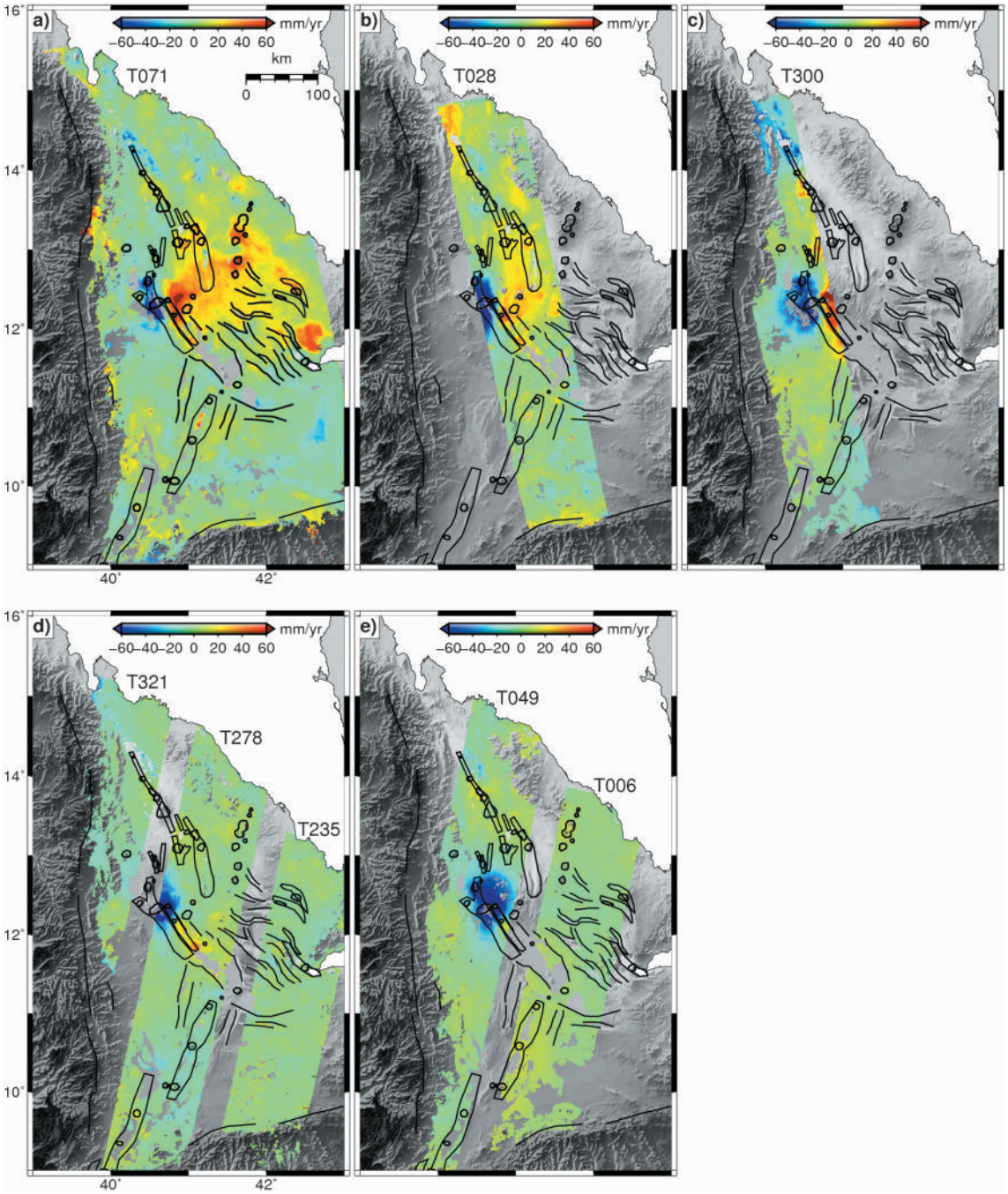

Figure 4. Average 2007–2010 LOS surface velocities for each InSAR track. The positive values indicate the range increase.

Ado Ale and Hararo magmatic systems are coeval and that an inverse correlation exists in the long-term (approximately years) velocity trends at the two sites, with uplift at Ado Ale coupled with subsidence at Hararo. These signals are decoupled from the dike intrusion processes occurring at shallow crustal depths and are likely caused by magma flow at deep crustal levels.

In this paper we aim at combining average InSAR velocity maps with GPS to obtain a 3-D velocity field. Regular GPS measurements near Dabbahu started only in 2007, and InSAR velocities have been approximately linear since that time (Figure 3). Therefore, we further calculated maps of average LOS InSAR velocities and associated RMS misfits for the 2007–2010 time period (Figure 4 and Figures S5–S9 in the supporting information) and use these to combine with the GPS. The InSAR velocities (Figure 4) show a consistent pattern with the

©2014. The Authors.

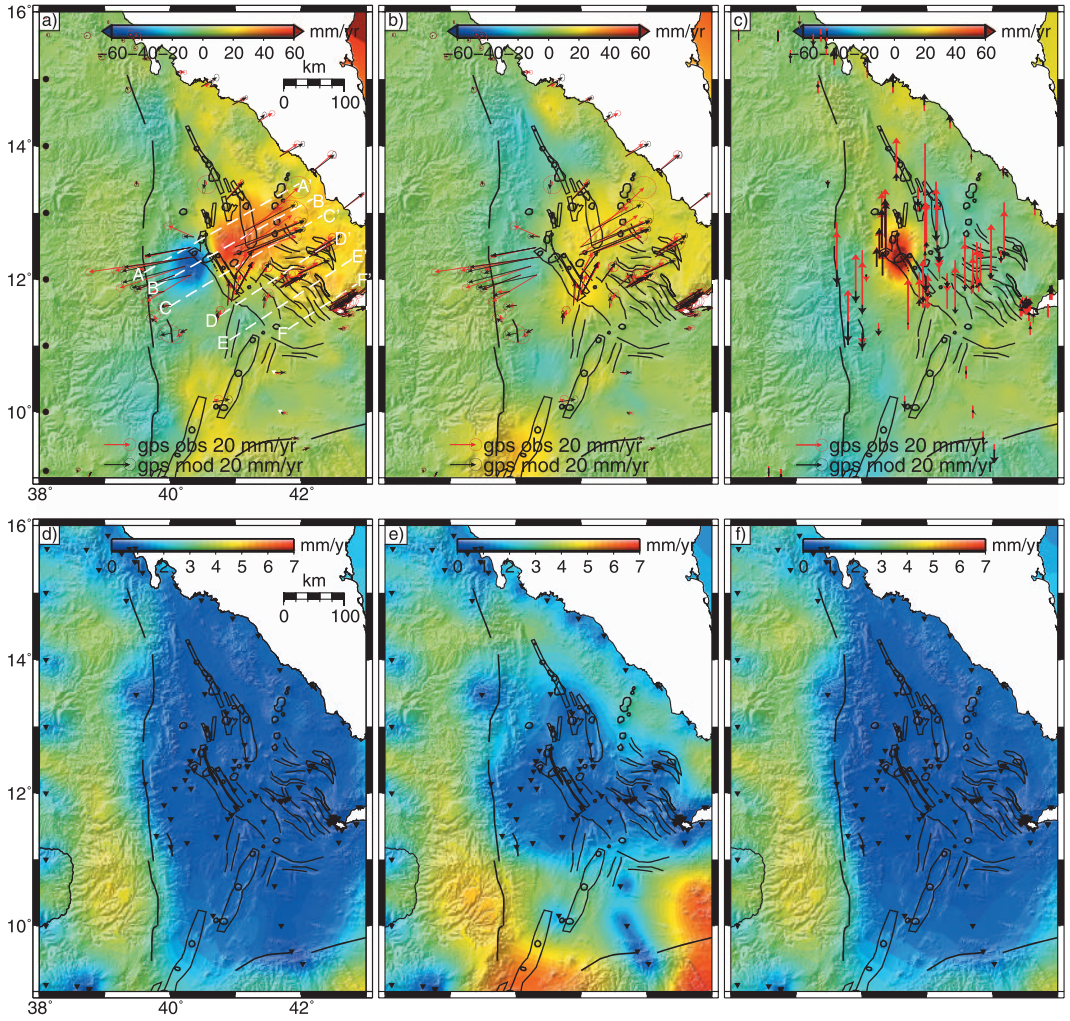

Figure 5. Continuous 3-D velocity field of Afar 2007–2010 and uncertainties. (a) Map of east-west surface velocity and overlapped GPS horizontal velocities relative to stable Nubia. The positive values indicate the movement toward east. (b) Map of north-south surface velocity and overlapped GPS horizontal velocities relative to stable Nubia. The positive values indicate the movement toward north. (c) Map of vertical surface velocity and overlapped GPS vertical velocities. The positive values indicate the uplift. (d) Map of the uncertainty on the east-west surface velocity. (e) Map of the uncertainty on the north-south surface velocity. (f) Map of the uncertainty on vertical surface velocity. The black inverted triangles mark the GPS stations.

largest deformation concentrated at the Dabbahu segment. There is a range decrease signal along the segment in all the tracks in spite of the different viewing geometries, indicating that most of this deformation is consistent with uplift. Subsidence at Hararo (range increase) is also clearly seen in different velocity maps. Another deformation signal consistent with subsidence is observed at the southern tip of the Dabbahu–Manda Hararo rift and is likely related to the exploitation of an aquifer [*Tessema*, 2013]. Although some obvious vertical motions can be identified in the InSAR velocity maps, horizontal motions remain challenging to extract using InSAR only. For this purpose, we combined our InSAR 2007–2010 velocity maps with the GPS to extract the three-dimensional velocity field.

4. 3-D Continuous Velocity Field

We combined the eight InSAR velocity maps (Figure 4) with the available GPS data to invert for the three-dimensional velocity field, using a method originally applied to GPS [*England and Molnar*, 2005] and adapted to GPS and InSAR by *Wang and Wright* [2012]. We divided the Afar region into a mesh of triangular elements with varying size and assumed that the velocity varies linearly with latitude and longitude within each triangle. Therefore, the geodetic observations (InSAR and GPS) within each triangle are related to the velocities of their

©2014. The Authors.

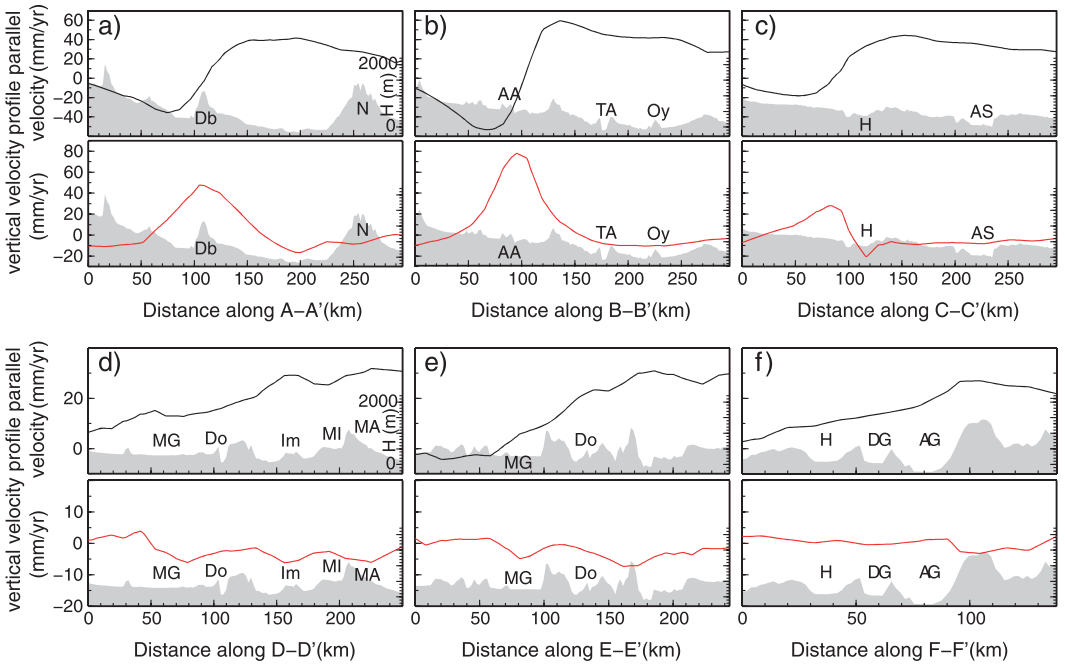

Figure 6. (a–f) Cross sections of surface velocities. Profile-parallel horizontal velocities (black lines) and vertical velocities (red lines). Cross section locations are shown in Figure 5a. The grey shading shows the topography, and the scale is read on the right-hand vertical axis of the figure, as in Figure 6a. The letters mark the rift segments and volcanoes as in Figure 1a.

vertices by an interpolation function. A denser mesh with nodes at ~10 km spacing is used at the rift axis and over volcanic segments, while progressively larger elements with node spacing of ~20 km are used in the far field. Prior to the inversion, we applied further multilooking to the line of sight velocity data sets, giving them a final pixel size of ~4.5 km. We used GPS velocities with respect to Nubia and assumed that velocities at a few points in the stable part of Nubia are equal to zero (black dots in Figure 5a). Since only a few GPS points are available on the Somalian Plate, the motion of this plate was poorly defined. We fixed the velocities at two additional points on the Somalian Plate (white inverted triangles in Figure 5a). At these points, we assumed velocities equal to the GPS points on the Somalian Plateau. As our fixed points in Somalia are far from active rift segments and the Nubia–Somalia extension is less than 10 mm/yr, this does not impact on the velocity field obtained within the Afar region. We inverted for the velocities of the triangular vertices using the system of equation described in *Wang and Wright* [2012] and including a quadratic model to fit orbital and long-wavelength atmospheric delay errors. The system of equations was solved using a least square method that included full variance-covariance matrices as well as smoothing with a Laplacian operator. We selected a smoothing factor that minimizes the trade-off between the solution roughness and the weighted RMS misfit of the models (Figure S10 in the supporting information). The RMS residual between the InSAR rate maps and the predictions from the velocity field is 7 mm/yr, while the GPS has a total residual of 9 mm/yr, with 4 mm/yr of residual in the east and north components and 15 mm/yr in the vertical. The RMS residuals are comparable to the uncertainty of the input data; therefore, the solution from our 3-D inversion finds a relatively good fit to the data. InSAR LOS observed, fitted, and residual velocities are shown in Figures S11–S15 in the supporting information. Some residual deformation mainly near Ado Ale and Dabbahu volcanoes is attributed to mesh size that is likely too coarse to accurately reproduce focused signals at volcanoes. Also, using a single smoothing factor for the whole region does not allow the inversion to fit every spatial wavelength of the deformation field, in particular at volcanoes, causing some residuals. After finding the velocities at the vertices of the triangles, we obtained a continuous velocity field by interpolation (Figures 5a–5c). Uncertainties on each component of the velocity field have also been calculated and are shown in Figures 5d–5f. For the velocity field inversion, we used GPS velocities with respect to Nubia; therefore, our final velocities are also in this reference system. Finally, we calculate the horizontal strain rates, coherent rotations, and their uncertainties at each vertex using spherical approximation equations (A6 in *Savage et al.* [2001]). Uncertainties are small compared to the displacement rates (Figures 5d–5f). The uncertainties on the

©2014. The Authors.

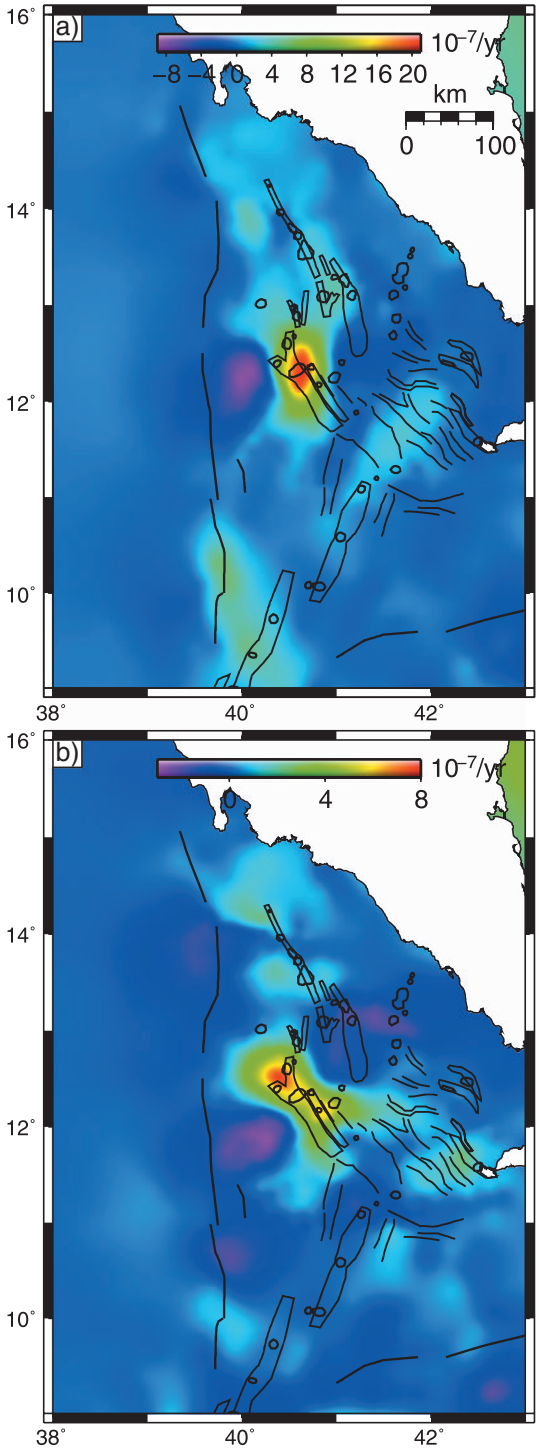

Figure 7. (a) Normal strain rate, $\dot{\varepsilon}_{xx}$. (b) Shear strain rate, $\dot{\varepsilon}_{xy}$.

east-west and vertical velocities are small over the entire Afar depression and do not exceed 4 mm/yr, with the largest values observed in the southern and western plateaus, where we lack InSAR observations due to loss of coherence. Larger uncertainties, up to 7 mm/yr, are observed in the north-south velocity. This is expected as the north-south motion is the least-well resolved by InSAR. The pattern of north-south uncertainties is alsolargely dependent on the GPS station distribution, with smaller uncertainties in central and southern Afar, where most GPS stations are located but larger uncertainties where GPS stations are sparse, such as in the Danakil Alps, the Somalian Plateau, the Main Ethiopian Rift, and the western plateau. Another reason for the generally smaller uncertainties in central and southern Afar is that most independent ascending and descending InSAR acquisitions are available in these areas.

The most prominent signals are the exceptionally fast extension across Dabbahu (Figure 5a) and the uplift centered at Ado Ale (Figure 5c). The east-west plate motions are also well resolved in southern and central Afar, allowing us to clearly define the location of the axis of the plate boundary, the width of the plate boundary deformation zone, as well as the rift segmentation. The highest extension rates and strain of Afar are ~110 mm/yr at Dabbahu and 20×10^{-7} strain/yr (Figure 5a, Figures 6a–6c, Figure 7a, and Figure 8a), as a result of postdiking processes. Extension is higher in the central part of the segment, at Ado Ale, and decays symmetrically at the segment tips (Figures 6a–6c). An analogous pattern is observed in the vertical velocities with values as high as 80 mm/yr in the center of the segment, at Ado Ale (Figure 5c and Figures 6a–6c). Since the horizontal velocities are not uniform along Dabbahu but decay toward the segment tips, this causes some shear (Figures 7b and 8b) as well as coherent rotations in the horizontal plane (Figure 9a). Coherent rotations about the *y* and *x* axes are also observed due to the vertical uplift in the center of the segment (Figures 9b and 9c). The strain and rotation rates (Figures 7–9) are significantly larger than the estimated uncertainties (Figures S16–S18) over the entire Afar depression and follow a pattern as also observed for the velocity field inversion (Figures 5c and 5d), with higher uncertainties in the southern and western plateaus.

To the north of Dabbahu, the rift axis steps over eastward across two zones of extension, the Erta Ale Ridge and Tat Ale (Figure 7a). Extension is observed across the Alayta segment as well (Figure 7a), but strains here are dominated by the nearby postdiking deformation at Dabbahu. Farther north along the Erta Ale Ridge (Figure 7a), the localization of the rift axis is less clear as extension rates decay due to the partitioning of the

©2014. The Authors.

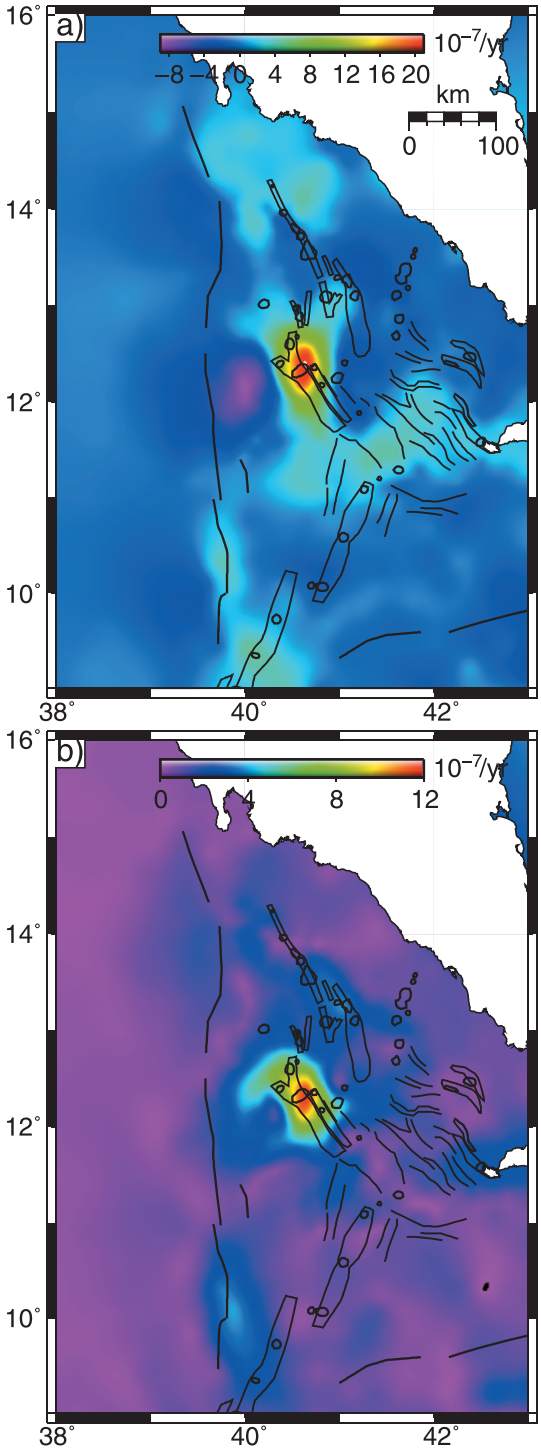

Figure 8. (a) First invariant of the horizontal strain rate tensor, also called dilatation or areal strain, positive values are extension. (b) Maximum horizontal shear strain rate.

spreading between the onland segment and the offshore Red Sea Rift. Furthermore, the paucity of GPS sites close to the rift axis does not allow us to fully describe the distribution of tectonic motions.

South of Dabbahu–Manda Hararo, extension is accommodated across a 150–200 km wide plate boundary deformation zone (PBZ) encompassing the Manda Gargori, Dobi, and Immino rifts (Figures 6d and 8a). A similarly broad accommodation zone is observed farther south with spreading distributed across Manda Gargori and Dobi in a PBZ about 150 km wide (Figures 6e and 8a). Strain is distributed over a much narrower area in the southeastern part of the plate boundary, where extension is mainly localized in Asal–Ghoubbet (Figures 6f and 8a) with only minor extension in Hanle and Derele–Gaggade and a PBZ of about 50 km width. Furthermore, no significant strain is observed at the Tendaho fault (Figures 7–9), suggesting that this structure is not currently active. However, motions of only a few mm/yr would not be resolved by our strain maps as the InSAR data spans a limited time period, 2007–2010. The row of volcanoes between Nabro and Oyma caldera also lacks significant strain (Figures 7 and 8), suggesting that these volcanoes do not currently mark an active portion of the plate boundary. Central volcanic activity, like the 2010 Nabro eruption [*Hamlyn et al.*, 2014], where we do not observe any precursory deformation, is likely associated with local magmatic processes similar to off-rift volcanoes.

5. Discussion and Conclusions

The novel cross-correlation method described in this work allows us to estimate and remove sudden deformation from intrusions and eruptions without using a priori source models or assuming a linear deformation rate. Another advantage of this method is that the residual signal can then be effectively cleaned from atmospheric noise during time series analysis, using both APS and smoothing. The minimization of atmospheric noise in the time series allows us to identify a sharp decrease in uplift rate in 2006 at Ado Ale coinciding to a subsidence decrease at Hararo. This observation has important implications for the mechanism of rifting as it implies that a direct connection between Ado Ale and Hararo likely exists. We suggest that a continuous magma flow from a distant part of the segment toward the Ado Ale chamber in the rift center occurs, contributing to the observed uplift. The inflation/deflation at Ado Ale and Hararo and the superimposed accelerated spreading have been modeled as viscoelastic stress relaxation and individual magma chambers [*Hamling et al.*, 2014]. However, a physical connection between

©2014. The Authors.

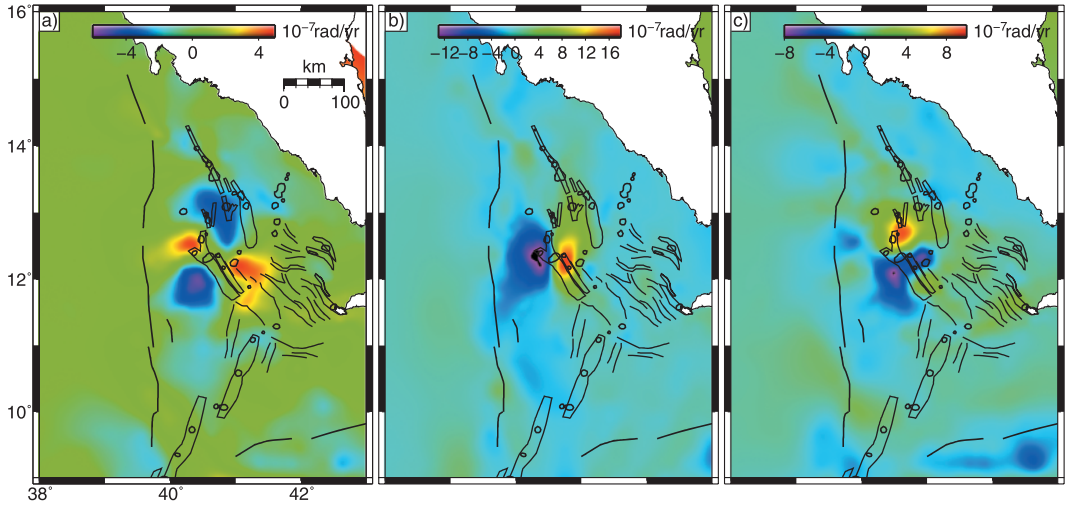

Figure 9. Coherent rotations: (a) Rotations about vertical axis, positive clockwise. (b) Rotations about *y* axis, positive toward east. (c) Rotations about *x* axis, positive toward north.

the two magma sources has not been proposed yet. We observe a segment-centered uplift of up to 80 mm/yr, indicating that magma flow is still a primary mechanism of deformation during the postdiking phase. On the other hand, no vertical displacements are currently observed in central and southern Afar, indicating lack of significant magmatic activity at shallow levels in these regions at present time.

Our three-dimensional velocity field provides for the first time a picture of the current plate boundary deformation in Afar, illustrating contrasted patterns and processes at work. The dominant signal is the transient postdiking deformation around Dabbahu, where melt migration between connected magma chambers and likely viscous relaxation occur. There, spreading velocities are about 6 times larger than the long-term averages of 18 mm/yr, and postdiking deformation affects a region that is about 200 km wide. In central Afar, extension is distributed over a broad (150–200 km) plate boundary zone including several overlapping rift segments. Interestingly, this region is devoid of active magmatic segments (Figure 1) and has the thickest crust in Afar, ~26 km [*Hammond et al.*, 2011; *Makris and Ginzburg*, 1987]. In contrast, we find that spreading is accommodated across a very narrow (<50 km) zone in southern Afar (Asal–Ghoubbet), where previous diking events occurred [*Cattin et al.*, 2005; *Vigny et al.*, 2007]. The width over which the plate boundary deformation is accommodated, as well as whether magmatic or tectonic processes are dominant, appears to vary along strike in Afar, probably reflecting the amount of crustal thinning and subcrustal melt available.

This differs from the more mature Iceland spreading center, where a PBZ ranging between 50 and 100 km is observed across all the spreading rift segments [*Árnadóttir et al.*, 2009; *LaFemina et al.*, 2005]. In Afar, less strain focus occurs at rift segments that are not known to have experienced diking events, like the Manda Gargori, Dobi, and Immino rifts. This is likely the result of the less mature stage of rifting of Afar, where continental rupture has not completely evolved to oceanic spreading. Plate spreading in Afar is achieved not only through episodic intrusions (i.e., diking events in Dabbahu and Asal–Ghoubbet) but also through diffuse crustal extension and normal faulting in areas of thicker and colder crust that have not experienced diking events, like the Manda Gargori, Dobi, and Immino rifts. This is also consistent with the seismicity of the area showing normal faulting mechanisms [*Keir et al.*, 2013; *Sigmundsson*, 1992] as well as thick crust and lower V_p/V_s ratio, suggesting lower degrees of melt than in other Afar rift segments [*Hammond et al.*, 2011]. These results should be an impetus for developing advanced deformation models explaining these coexisting behaviors over distinct rift segments, possibly representative of different evolutionary phases of the transition from continental rupture to oceanic spreading. Figure 10 shows a schematic view of the different modes of strain accommodation in the Afar rift segments. Figure 10a depicts a typical rift segment that has evolved through repeated rifting events and magma intrusions, such as Dabbahu but also Asal–Ghoubbet, while Figure 10b shows two overlapping rift segments with a widespread strain accommodation area, where deformation is dominated by faulting, and it is lacking a system of intrusions as created during rifting events. This mode of deformation is observed at the Manda Gargori, Dobi, and Immino rifts.

©2014. The Authors.

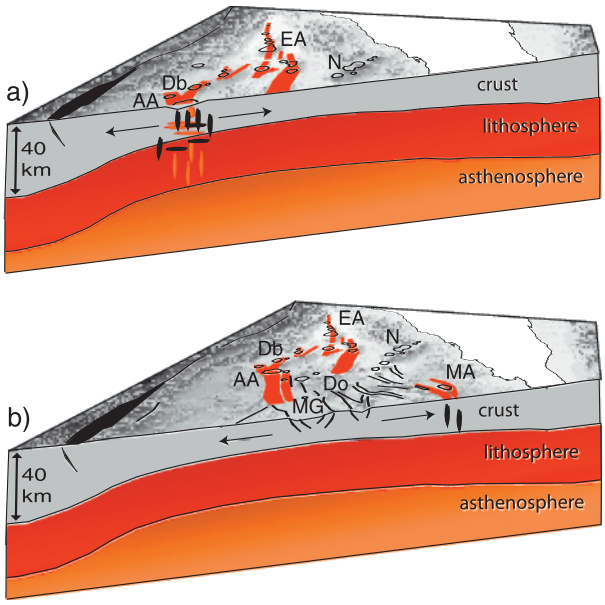

Figure 10. Cartoon of the different modes of strain accommodation in the Afar rift segments. (a) Rift segment that has evolved through rifting events and repeated magma intrusions, such as Dabbahu. (b) Extension accommodated by faulting, lacking a system of intrusions as created during rifting events, but causing a widespread strain accommodation area as in the Manda–Gargori and Dobi grabens.

Our strain maps also show coherent horizontal rotations about a vertical axis in the area around Dabbahu due to the segment-centered accelerated extension (Figure 9a). Although we cannot reconstruct the long-term rotation pattern in Afar as we lack detailed knowledge about past diking events, our results show that the pattern of postdiking deformation can induce coherent rotations, providing another possible way of explaining the paleomagnetic block rotations observed in Afar [*Kidane et al.*, 2003].

Using our three-dimensional velocity field and strain maps, we identified the main areas of plate boundary deformation as well as the rift segmentation in Afar. As the Gulf of Aden rift becomes onland in Djibouti, extensions are confined to the Asal–Ghoubbet rift. The plate boundary then steps over westward across the Manda Gargori, Dobi, and Immino grabens, and then reconnects to the Dabbahu–Manda Hararo rift. The absence of significant strain along the Nabro and Oyma row of calderas but also at Moussa–Alli and Manda–Inakir Inakir suggests that these structures are less active than previously thought and that extension and magmatic activity have shifted toward the western rift segments. This is also in agreement with seismic tomography results showing areas of low velocities interpreted as zones of passive mantle upwelling underneath the western rifts, while no significant anomalies are observed in the eastern rifts [*Hammond et al.*, 2013]. A similar scenario has also occurred in Iceland where rifting jumped eastward from the Snaefellsnes, western and eastern rifting zones [*Sigmundsson*, 2006].

Acknowledgments

C.P. thanks Peng Li and Zhenhong Li for their support with the wide swath processing software. C.P. gratefully acknowledges the support she receives through her Rita Levi Montalcini fellowship (Nota MIUR Montalcini 26259_21/12/2013). This work was supported by the UK National Environment Research Council NERC NE/D008611/1, NE/D01039X/1, and NE/E007414/1 grants and the Centre for the Observation and Modelling of Earthquakes, Volcanoes, and Tectonics. H.W. was supported by the National Natural Science Foundation of China grants 41104016 and 41372221. E.C. acknowledges support from NSF grants EAR-0635789 and EAR-0613651 and from JPL subcontract 148113. The SAR data used to produce all interferograms are copyright to ESA from CAT 1 3435. All processed interferograms are archived at the University of Leeds (contact T.J.Wright@leeds.ac.uk), and all the GPS data and station velocities are archived at Ecole Normale Superieure (contact eric.calais@ens.fr). The π-rate software developed by Hua Wang and used for the time series analysis is freely available online (http://homepages.see.leeds.ac.uk/~earhw/software/pi-rate/index.html).

References

Árnadóttir, T., B. Lund, W. Jiang, H. Geirsson, H. Björnsson, P. Einarsson, and T. Sigurdsson (2009), Glacial rebound and plate spreading: Results from the first countrywide GPS observations in Iceland, *Geophys. J. Int.*, *177*(2), 691–716.

Barberi, F., and J. Varet (1977), Volcanism of Afar - Small-Scale Plate Tectonics Implications, *Geol. Soc. Am. Bull.*, *88*(9), 1251–1266.

Biggs, J., T. Wright, Z. Lu, and B. Parsons (2007), Multi-interferogram method for measuring interseismic deformation: Denali fault, Alaska, *Geophys. J. Int.*, *170*(3), 1165–1179.

Cattin, R., C. Doubre, J. B. de Chabalier, G. King, C. Vigny, J. P. Avouac, and J. C. Ruegg (2005), Numerical modelling of quaternary deformation and post-rifting displacement in the Asal-Ghoubbet rift (Djibouti, Africa), *Earth Planet. Sci. Lett.*, *239*(3–4), 352–367.

Courtillot, V. E. (1980), Opening of the Gulf of Aden and Afar by progressive tearing, *Phys. Earth Planet. Inter.*, *21*(4), 343–350.

Ebinger, C., A. Ayele, D. Keir, J. Rowland, G. Yirgu, T. Wright, M. Belachew, and I. Hamling (2010), Length and Timescales of Rift Faulting and Magma Intrusion: The Afar Rifting Cycle from 2005 to Present, *Annu. Rev. Earth Planet. Sci.*, *38*(1), 439–466.

Elliott, J. R., J. Biggs, B. Parsons, and T. J. Wright (2008), InSAR slip rate determination on the Altyn Tagh Fault, northern Tibet, in the presence of topographically correlated atmospheric delays, *Geophys. Res. Lett.*, *35*, L12309, doi:10.1029/2008GL033659.

England, P., and P. Molnar (2005), Late Quaternary to decadal velocity fields in Asia, *J. Geophys. Res.*, *110*, B12401, doi:10.1029/2004JB0003541.

Ferretti, A., C. Prati, and F. Rocca (2001), Permanent scatterers in SAR interferometry, *IEEE Trans. Geosci. Remote*, *39*(1), 8–20.

Field, L., T. Barnie, J. Blundy, R. A. Brooker, D. Keir, E. Lewi, and K. Saunders (2012), Integrated field, satellite and petrological observations of the November 2010 eruption of Erta Ale, *Bull. Volcanol.*, *74*(10), 2251–2271.

Foulger, G. R., C. H. Jahn, G. Seeber, P. Einarsson, B. R. Julian, and K. Heki (1992), Post-Rifting Stress-Relaxation at the Divergent Plate Boundary in Northeast Iceland, *Nature*, *358*(6386), 488–490.

Grandin, R., A. Socquet, M. P. Doin, E. Jacques, J. B. de Chabalier, and G. C. P. King (2010), Transient rift opening in response to multiple dike injections in the Manda Hararo rift (Afar, Ethiopia) imaged by time-dependent elastic inversion of interferometric synthetic aperture radar data, *J. Geophys. Res.*, *115*, B09403, doi:10.1029/2009JB006883.

Hamling, I. J., T. J. Wright, E. Calais, E. Lewi, and Y. Fukahata (2014), InSAR observations of post-rifting deformation around the Dabbahu rift segment, Afar, Ethiopia, *Geophys. J. Int.*, *197*(1), 33–49.

Hamlyn, J. E., D. Keir, T. J. Wright, J. W. Neuberg, B. Goitom, J. O. S. Hammond, C. Pagli, C. Oppenheimer, and J. M. Kendall (2014), Seismicity and subsidence following the 2011 Nabro eruption, Eritrea: Insights into the plumbing system of an off-rift volcano, *J. Geophys. Res. Solid Earth*, doi:10.1002/2014JB011395.

©2014. The Authors.

Hammond, J. O. S., J. M. Kendall, G. W. Stuart, D. Keir, C. Ebinger, A. Ayele, and M. Belachew (2011), The nature of the crust beneath the Afar triple junction: Evidence from receiver functions, *Geochem. Geophys. Geosyst.*, *12*, Q12004, doi:10.1029/2011GC003738.
Hammond, J. O. S., et al. (2013), Mantle upwelling and initiation of rift segmentation beneath the Afar Depression, *Geology*, *41*(6), 635–638.
Hanssen, R. F. (2001), *Radar Interferometry: Data Interpretation and Error Analysis*, 328 pp., Kluwer Acad. Publ., Dordrecht, Netherlands.
Heki, K., G. R. Foulger, B. R. Julian, and C. H. Jahn (1993), Plate Dynamics near Divergent Boundaries - Geophysical Implications of Postrifting Crustal Deformation in Ne Iceland, *J. Geophys. Res.*, *98*(B8), 14,279–14,297.
Hofton, M. A., and G. R. Foulger (1996), Postrifting anelastic deformation around the spreading plate boundary, north Iceland. 1. Modeling of the 1987–1992 deformation field using a viscoelastic Earth structure, *J. Geophys. Res.*, *101*(B11), 25,403–25,421.
Keir, D., I. D. Bastow, C. Pagli, and E. L. Chambers (2013), The development of extension and magmatism in the Red Sea rift of Afar, *Tectonophysics*, *607*, 98–114.
Kidane, T., V. Courtillot, I. Manighetti, L. Audin, P. Lahitte, X. Quidelleur, P. Y. Gillot, Y. Gallet, J. Carlut, and T. Haile (2003), New paleomagnetic and geochronologic results from Ethiopian Afar: Block rotations linked to rift overlap and propagation and determination of a similar to 2 Ma reference pole for stable Africa, *J. Geophys. Res.*, *108*(B2), 2102, doi:10.1029/2001JB000645.
Kogan, L., S. Fisseha, R. Bendick, R. Reilinger, S. McClusky, R. King, and T. Solomon (2012), Lithospheric strength and strain localization in continental extension from observations of the East African Rift, *J. Geophys. Res.*, *117*, B03402, doi:10.1029/2011JB008516.
Kruskal, J. B. (1956), On the shortest spanning subtree of a graph and the traveling salesman problem, *Proc. Am. Math. Soc.*, *7*(1), 48–50.
LaFemina, P. C., T. H. Dixon, R. Malservisi, T. Arnadottir, E. Sturkell, F. Sigmundsson, and P. Einarsson (2005), Geodetic GPS measurements in south Iceland: Strain accumulation and partitioning in a propagating ridge system, *J. Geophys. Res.*, *110*, B11405, doi:10.1029/2005JB003675.
Makris, J., and A. Ginzburg (1987), The Afar Depression: Transition between continental rifting and sea-floor spreading, *Tectonophysics*, *141*(1–3), 199–214.
Manighetti, I., P. Tapponnier, P. Y. Gillot, E. Jacques, V. Courtillot, R. Armijo, J. C. Ruegg, and G. King (1998), Propagation of rifting along the Arabia-Somalia plate boundary: Into Afar, *J. Geophys. Res.*, *103*(B3), 4947–4974.
McClusky, S., et al. (2010), Kinematics of the southern Red Sea-Afar Triple Junction and implications for plate dynamics, *Geophys. Res. Lett.*, *37*, L05301, doi:10.1029/2009GL041127.
Nobile, A., C. Pagli, D. Keir, T. J. Wright, A. Ayele, J. Ruch, and V. Acocella (2012), Dike-fault interaction during the 2004 Dallol intrusion at the northern edge of the Erta Ale Ridge (Afar, Ethiopia), *Geophys. Res. Lett.*, *39*, L19305, doi:10.1029/2012GL053152.
Nooner, S. L., L. Bennati, E. Calais, W. R. Buck, I. J. Hamling, T. J. Wright, and E. Lewi (2009), Post-rifting relaxation in the Afar region, Ethiopia, *Geophys. Res. Lett.*, *36*, L21308, doi:10.1029/2009GL040502.
Pagli, C., T. J. Wright, C. J. Ebinger, S. H. Yun, J. R. Cann, T. Barnie, and A. Ayele (2012), Shallow axial magma chamber at the slow-spreading Erta Ale Ridge, *Nat. Geosci.*, *5*(4), 284–288.
Rosen, P. A., S. Hensley, G. Peltzer, and M. Simons (2004), Updated repeat orbit interferometry package released, *Eos Trans. AGU*, *85*(5), 47–47, doi:10.1029/2004EO050004.
Saria, E., E. Calais, Z. Altamimi, P. Willis, and H. Farah (2013), A new velocity field for Africa from combined GPS and DORIS space geodetic Solutions: Contribution to the definition of the African reference frame (AFREF), *J. Geophys. Res. Solid Earth*, 1677–1697, doi:10.1002/jgrb.50137.
Saria, E., E. Calais, D. S. Stamps, D. Delvaux, and C. J. H. Hartnady (2014), Present-day kinematics of the East African Rift, *J. Geophys. Res. Solid Earth*, 3584–3600, doi:10.1002/2013JB010901.
Savage, J. C., W. J. Gan, and J. L. Svarc (2001), Strain accumulation and rotation in the Eastern California Shear Zone, *J. Geophys. Res.*, *106*(B10), 21,995–22,007.
Sigmundsson, F. (1992), Tectonic Implications of the 1989 Afar Earthquake Sequence, *Geophys. Res. Lett.*, *19*(9), 877–880.
Sigmundsson, F. (2006), *Iceland Geodynamics, Crustal Deformation and Divergent Plate Tectonics*, 209 pp., Praxis-Springer, Chichester, U. K.
Tapponnier, P., R. Armijo, I. Manighetti, and V. Courtillot (1990), Bookshelf faulting and horizontal block rotations between overlapping rifts in southern Afar, *Geophys. Res. Lett.*, *17*(1), 1–4.
Tessema, T. (2013), Deformation measurnment in Central Afar, Ethiopia uisng InSAR and GPS, Addis Abeba Univ., Addis Abeba, Ethiopia.
Vigny, C., P. Huchon, J. C. Ruegg, K. Khanbari, and L. M. Asfaw (2006), Confirmation of Arabia plate slow motion by new GPS data in Yemen, *J. Geophys. Res.*, *111*, B02402, doi:10.1029/2004JB003229.
Vigny, C., J. B. de Chabalier, J. C. Ruegg, P. Huchon, K. L. Feigl, R. Cattin, L. Asfaw, and K. Kanbari (2007), Twenty-five years of geodetic measurements along the Tadjoura-Asal rift system, Djibouti, East Africa, *J. Geophys. Res.*, *112*, B06410, doi:10.1029/2004JB003230.
Wang, H., and T. J. Wright (2012), Satellite geodetic imaging reveals internal deformation of western Tibet, *Geophys. Res. Lett.*, *39*, L07303, doi:10.1029/2012GL051222.
Wang, H., T. J. Wright, and J. Biggs (2009), Interseismic slip rate of the northwestern Xianshuihe fault from InSAR data, *Geophys. Res. Lett.*, *36*, L03302, doi:10.1029/2008GL036560.
Wang, H., T. J. Wright, Y. P. Yu, H. Lin, L. L. Jiang, C. H. Li, and G. X. Qiu (2012), InSAR reveals coastal subsidence in the Pearl River Delta, China, *Geophys. J. Int.*, *191*(3), 1119–1128.
Wright, T. J., B. E. Parsons, and Z. Lu (2004), Toward mapping surface deformation in three dimensions using InSAR, *Geophys.Res. Lett.*, *31*, L01607, doi:10.1029/2003GL018827.
Wright, T. J., C. Ebinger, J. Biggs, A. Ayele, G. Yirgu, D. Keir, and A. Stork (2006), Magma-maintained rift segmentation at continental rupture in the 2005 Afar dyking episode, *Nature*, *442*(7100), 291–294.
Wright, T. J., et al. (2012), Geophysical constraints on the dynamics of spreading centres from rifting episodes on land, *Nat. Geosci.*, *5*(4), 242–250.

©2014. The Authors.